

Title	Doping of ultra-thin Si films: Combined first-principles calculations and experimental study
Authors	Gity, Farzan;Meaney, Fintan;Curran, Anya;Hurley, Paul K.;Fahy, Stephen B.;Duffy, Ray;Ansari, Lida
Publication date	2021-01-04
Original Citation	Gity, F., Meaney, F., Curran, A., Hurley, P. K., Fahy, S., Duffy, R. and Ansari, L. (2021) 'Doping of ultra-thin Si films: Combined first-principles calculations and experimental study', Journal of Applied Physics, 129(1), 015701 (10 pp). doi: 10.1063/5.0035693
Type of publication	Article (peer-reviewed)
Link to publisher's version	https://aip.scitation.org/doi/10.1063/5.0035693 - 10.1063/5.0035693
Rights	© 2021 Author(s). All article content, except where otherwise noted, is licensed under a Creative Commons Attribution (CC BY) license - https://creativecommons.org/licenses/by/4.0/
Download date	2023-05-05 23:34:17
Item downloaded from	http://hdl.handle.net/10468/10864

Doping of ultra-thin Si films: Combined first-principles calculations and experimental study ^F

Cite as: J. Appl. Phys. **129**, 015701 (2021); <https://doi.org/10.1063/5.0035693>

Submitted: 30 October 2020 . Accepted: 29 November 2020 . Published Online: 04 January 2021

^{id} Farzan Gity, Fintan Meaney, ^{id} Anya Curran, ^{id} Paul K. Hurley, Stephen Fahy, ^{id} Ray Duffy, and ^{id} Lida Ansari

COLLECTIONS

^F This paper was selected as Featured



View Online



Export Citation



CrossMark



Your Qubits. Measured.

Meet the next generation of quantum analyzers

- Readout for up to 64 qubits
- Operation at up to 8.5 GHz, mixer-calibration-free
- Signal optimization with minimal latency

Find out more



Doping of ultra-thin Si films: Combined first-principles calculations and experimental study

Cite as: J. Appl. Phys. **129**, 015701 (2021); doi: [10.1063/5.0035693](https://doi.org/10.1063/5.0035693)

Submitted: 30 October 2020 · Accepted: 29 November 2020 ·

Published Online: 4 January 2021



Farzan City,  Fintan Meaney, Anya Curran,  Paul K. Hurley,  Stephen Fahy, Ray Duffy,  and Lida Ansari^{a)} 

AFFILIATIONS

Tyndall National Institute, University College Cork, Lee Maltings, Dyke Parade, Cork T12 R5CP, Ireland

^{a)}Author to whom correspondence should be addressed: Lida.Ansari@Tyndall.ie

ABSTRACT

This paper presents comprehensive density functional theory-based simulations to understand the characteristics of dopant atoms in the core and on the surface of ultra-thin sub-5 nm Si films. Quantum confinement-induced bandgap widening has been investigated for doped Si films considering two different doping concentrations. Thickness-dependent evolution of dopant formation energy is also extracted for the thin films. It is evident from the results that doping thinner films is more difficult and that dopant location at the surface is energetically more favorable compared to core dopants. However, the core dopant generates a higher density of states than the surface dopant. Projecting the carrier states in the doped Si film onto those of a reference intrinsic film reveals dopant-induced states above the conduction band edge, as well as perturbations of the intrinsic film states. Furthermore, to experimentally evaluate the *ab initio* predictions, we have produced *ex situ* phosphorus-doped ultra-thin-Si-on-oxide with a thickness of 4.5 nm by the beam-line ion implantation technique. High-resolution transmission electron microscopy has confirmed the thickness of the Si film on oxide. Transfer length method test structures are fabricated, and the temperature-dependent electrical characterization has revealed the effective dopant activation energy of the ion-implanted phosphorus dopant to be ≤ 13.5 meV, which is consistent with our theoretical predictions for comparable film thickness. Ultra-thin Si films are essential in the next generation of Si-based electronic devices, and this study paves the way toward achieving that technology.

© 2021 Author(s). All article content, except where otherwise noted, is licensed under a Creative Commons Attribution (CC BY) license (<http://creativecommons.org/licenses/by/4.0/>). <https://doi.org/10.1063/5.0035693>

INTRODUCTION

The conventional idea of using a fixed material set and scaling devices in length as expressed by Moore's "law"¹ to reduce costs while enhancing the performance, i.e., "Dennard scaling," came to an end effectively during the mid-1990s for the manufacture of integrated circuits relying on field-effect transistors (FETs). Since then, various technology boosters have been introduced including the introduction of new material sets in the gate stack to reduce gate tunneling, the use of strain engineering to enhance electron and hole mobility, and the use of silicon-on-insulators or "fin"-FETs to reduce short channel effects.^{2,3} Enormous efforts to overcome fundamental limitations associated with the physical behavior of materials and devices have been made, and more radical changes in device design are required. In the past several decades, the performance improvement of electronic devices is mainly satisfied by reducing the size of the silicon FETs.

For the "end-of-the-roadmap,"⁴ transistors are being scaled down to dimensions comparable to the Fermi wavelength.⁵ In such dimensions, the number of atoms is in the order of a few hundreds to thousands, i.e., nanometer scale. Nanoscale FETs enable the continuation of Moore's law for future technology generations, permitting higher device density and consequently higher function per integrated circuit at lower unit cost. In 2018, the semiconductor industry crossed the 10 nm threshold to offer Si-based logic technologies at the 7 nm technology node, with the 5 nm and 3 nm nodes expected in the foreseeable future.^{6–8} Exciting research is being carried out theoretically and experimentally consistently demonstrating that Si-based logic switches could be scaled down to the 3 nm node while maintaining high performance.^{9,10} In addition to logic devices, a new era of scalable quantum information processing and quantum neuromorphic device platforms is emerging based on ultra-low-dimension Si structures.^{11–17}

Among fundamental challenges of such scaling are (1) quantum confinement effects and (2) the small number of atoms in the transistor. Quantum confinement plays a considerable role in the electronic structure of the semiconductor, altering the “bulk” properties of the material, in particular, widening the semiconductor bandgap. On the other hand, the small number of atoms in the transistor channel makes doping the semiconductor even further challenging, since substituting just one atom can drastically modify its conductivity.^{18,19} Conductivity is one of the fundamental properties of a semiconductor, affecting the device performance, which can be controlled by intentional doping. Exciting progress has been achieved toward the realization of electronic devices at scales approaching fundamental limits set by atom sizes. Ultra-thin Si films have drawn considerable attention, particularly for fin-type and silicon-on-insulator (SOI) device technologies.^{8,20} There have been extensive theoretical and experimental studies on doping of Si nanostructures over the last two decades focusing, in particular, on Si nanowires and nanocrystals, corresponding to 1D and 0D nanostructures, respectively.^{21–27} Nevertheless, very limited studies have been reported on doping ultra-thin Si films; hence, it is vital and timely to systematically investigate the physical phenomena involved in doping Si thin films through a combined theoretical and experimental study.

In this study, we have performed *ab initio* simulations for a variety of ultra-thin Si films considering two different phosphorus doping concentrations. In order to provide insight into the dopant band, we have also considered Si nanowires with a diameter of 1 nm. Different nanowire lengths are taken into account allowing nanowire structures with various doping concentrations. This allows the dopant band to clearly appear in the bandgap, depending on the doping concentration. We have also experimentally n-type doped SOI wafers by phosphorus ion implantation. The exact thickness of the Si film is verified to be 4.5 nm by cross-sectional transmission electron microscopy (XTEM). Temperature-dependent electrical characterization is performed on circular transfer length method (CTLTM) structures to extract the activation energy of the dopants.²⁸

AB INITIO SIMULATIONS

Low-dimensional Si films with 1.2 nm, 2.2 nm, 3.3 nm, and 4.4 nm thickness, and Si nanowires (NWs) with a diameter of 1 nm and different lengths of 1.2 nm, 2.3 nm, 3.5 nm, 4.6 nm, and 5.8 nm, are considered in this modeling study. To obtain the electronic structure of the Si films and NWs, density functional theory (DFT) calculations are performed as implemented in QuantumATK.²⁹ Norm-conserving pseudopotentials as parametrized by Perdew Zunger with local density approximation (LDA) are employed.³⁰ *S3p3d1*, *s2p2*, and *s3p3d1* numerical atomic orbital basis sets are considered for Si, hydrogen, and phosphorus, respectively.^{31–33} Geometry optimization is performed by minimizing the total energy with respect to atomic positions to achieve the maximum force of ≤ 0.02 eV Å⁻¹. 90 Hartree has been considered as the energy cutoff. Monkhorst–Pack k-point grids³⁴ have been used for Brillouin-zone integrations with a density of ~ 10 k-points/Å along the periodic axes. Underestimation of the bandgap energies is typical when employing common exchange-correlation functionals in the DFT calculations. Therefore, to achieve a more precise estimation of the bandgap energies for the relaxed DFT–LDA geometries,

meta-generalized gradient approximation (meta-GGA) exchange-correlation functional³⁵ is utilized. It has been revealed that meta-GGA provides bandgap values comparable to the experimental data for many semiconductors, if properly calibrated. In addition, meta-GGA also results in an improved description of the bulk and two-dimensional electronic structure of the semiconductor.³⁵ It is important to point out that the abovementioned DFT parameters describe the band structure of bulk Si in very good agreement with the experiment, as shown in Fig. S1 in the [supplementary material](#).

As discussed in the “Experimental investigation” section, the last step in our process of doping Si thin film is exposing the Si surface to hydrofluoric (HF) acid. Therefore, in constructing the atomic structures, dangling bonds at the surface of Si films and NWs are passivated using hydrogen (–H) atoms to obtain stable minimum energy. Periodic boundary conditions are applied in creating the simulation supercells. The cell dimension transverse to the film surface is chosen to be greater than 2 nm to reduce the interaction between the periodic images of neighboring films. Film thickness is defined as the distance between the lower and upper hydrogen passivating atoms. The band structure of Si [100] slabs, consistent with our experimental wafer orientation, with thicknesses from 1.2 nm to 4.4 nm, is shown in Fig. 1. The bandgap increases with decreasing film thickness, from 1.17 eV for the 4.4 nm film to 1.72 eV for the 1.2 nm film, consistent with an intuitive picture of the quantum confinement. In other words, going from (a) through (d), as the film becomes thicker, the discretization of the wave vector perpendicular to the film becomes less well-defined and there are a lower number of states compared to thicker films as it gets closer to the so-called “projected bulk band structure” for the 4.4 nm film. As can be conspicuously seen in Fig. 1, the energy state at Γ -minimum has not changed much compared to other states at around M-minimum. Given the [100] orientation of the film, the Δ -line in the (100) direction of the bulk Brillouin-zone projects onto the Γ -point in the surface of the Brillouin zone. Therefore, film states derived from bulk states near the Δ conduction band minimum (CBM) along the (100) direction appear at Γ in the surface Brillouin zone shown, whereas states that are derived from the Δ band minima along the (010) and (001) directions appear near M in the surface Brillouin zone. Since the longitudinal effective mass at the Δ bulk band minimum is much greater than the transverse mass, the states at the (010) and (001) band minima are raised by quantum confinement in the [100] slab much more than those at the (100) band minimum. This will be referred back to while discussing about the formation of dopant band in Fig. 5.

Band structure and bandgap value of the Si thin films are modified by the quantum confinement and surface termination. Similar to other materials, Si ultra-thin films with no surface termination have zero bandgap while passivating the surface opens up the gap.^{36,37} Hydrogen (–H)-terminated Si films show larger bandgap values compared to hydroxyl (–OH)-terminated films, while opposite behavior has been observed in Bi ultra-thin films.^{38,39} Band structures of –OH-terminated 3.3 nm- and 4.4 nm-thick films are presented in Fig. S2 in the [supplementary material](#) showing bandgap values of 1.17 eV and 1.13 eV, respectively. The impact of the surface termination on Si films is less pronounced compared to Si nanostructures^{40–43} due to a larger surface-to-volume ratio. As can be seen from Fig. 1, the valence band maximum (VBM) and the

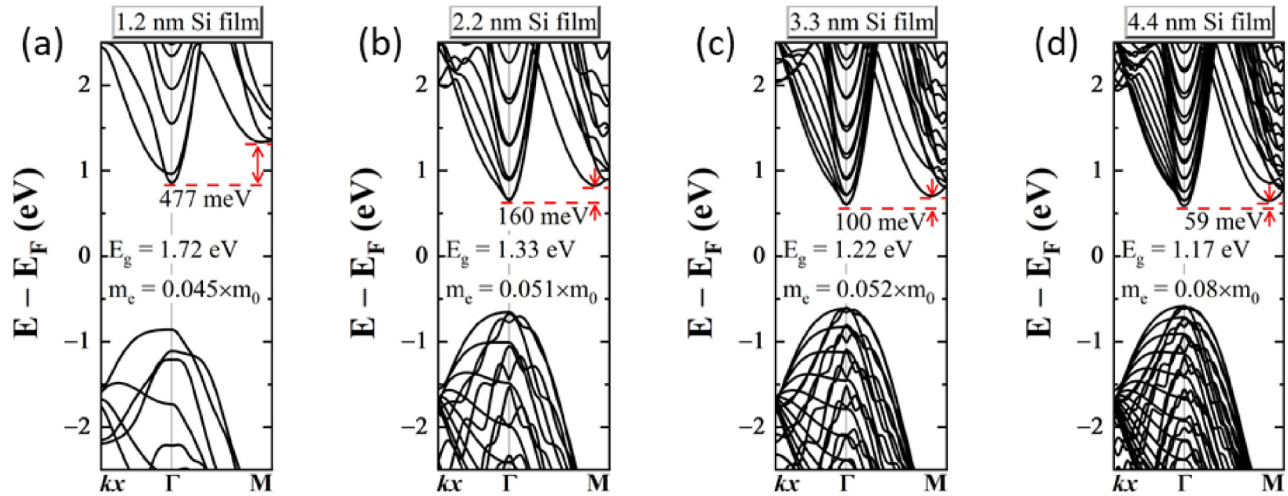


FIG. 1. Band structure of intrinsic Si ultra-thin films. Hydrogen-terminated Si films along [100] orientation and thickness of (a) 1.2 nm, (b) 2.2 nm, (c) 3.3 nm, and (d) 4.4 nm. E_g and m_e are bandgap and electron effective mass, respectively. Red arrows show the energy difference between the two conduction band minima. Energies are referenced to the Fermi level (E_F). kx represents the edge of the Brillouin zone in the x -direction.

conduction band minimum (CBM) is located at Γ for all of the Si thin films. In other words, all the Si films considered in this study are direct bandgap as a result of quantum confinement, which can be further explored in silicon photonics, in particular, Si-based light sources.^{44,45} The off- Γ CBM is pushed up for the 1.2 nm film by ~ 0.48 eV; however, it is just ~ 60 meV above the Γ -point CBM for the 4.4 nm film. The electron effective mass, denoted by m_e , also shows a reducing trend as the film thickness decreases. In other words, while the bandgap widens due to quantum confinement, not only does the Si film become direct gap material, but the curvature of the conduction band increases, and hence, the effective mass decreases.

To investigate the properties of the doped Si films and to allow fair comparison between films with different thicknesses, we have considered approximately 400 Si atoms per dopant atom in the supercell, corresponding to the doping concentration of $1.2 \times 10^{20} \text{ cm}^{-3}$. As a result, different supercell dimensions of approximately $2.7 \times 2.7 \text{ nm}^2$, $2 \times 2 \text{ nm}^2$, $1.5 \times 1.5 \text{ nm}^2$, and $1.5 \times 1.14 \text{ nm}^2$ along the two periodic axes of the supercell are considered for the 1.2 nm, 2.2 nm, 3.3 nm, and 4.4 nm thick slabs, respectively. Silicon technology is now approaching a scale at which both the number and location of individual dopant atoms within a device will determine its characteristics.^{46,47} Hence, in this study, we consider different locations of phosphorus—a key dopant atom not only for conventional logic devices but also for Si-based qubit logic gate⁴⁸—in the Si films: substituting one of the innermost Si atoms with a phosphorus atom is a “core dopant,” and substituting one of the outermost Si atom a “surface dopant.”⁴⁹ It is worth mentioning that the number of impurities required for the synthesis of doped nanostructures could be orders of magnitude more than the bulk structures.^{47,50} Atomic illustration of the doped Si thin films—core dopant—is shown in Fig. 2, for the four different film thicknesses. As mentioned above, the volume per dopant is kept

constant, and, therefore, the planar distance between dopants decreases with increasing film thickness. The conduction band structures of the Si thin films with the doping concentration of $1.2 \times 10^{20} \text{ cm}^{-3}$ (corresponding to approximately 400 Si atoms per dopant atom) are also shown in Fig. 2 for each film thickness and dopant location, illustrating core and surface dopant situations. For this doping concentration, all the films are degenerate, and the Fermi level is well inside the conduction band (energies are referenced to the Fermi level). As can be conspicuously seen, quantum-confinement-induced bandgap widening, which is more pronounced in thinner films, leads to less degeneracy in the thinner films. This explains the technological bottleneck for the next generation of ultra-thin-film technologies, such as uSOI and fin-FET transistors, where, as the film gets thinner, doping becomes increasingly challenging.⁵¹ As can also be seen in Fig. 2, the surface dopant provides a lower density of states (DoS) at energies close to the Fermi level. DoS of the 4.4 nm thin film is shown in Fig. S3 in the [supplementary material](#) for both the surface and the core dopant locations.

In order to compare the relative degree of difficulty for a dopant atom to be incorporated into the Si thin film, the impurity formation energy (E_{form}) is analyzed and extracted using

$$E_{\text{form}} = (E_{\text{doped-Si}} - E_{\text{i-Si}}) + n \cdot (\mu_{\text{Si}} - \mu_{\text{dopant}}), \quad (1)$$

where $E_{\text{doped-Si}}$ is the total energy of a doped Si film and $E_{\text{i-Si}}$ is the total energy of the corresponding intrinsic Si film. μ_{Si} and μ_{dopant} are the chemical potentials of Si and phosphorus dopant atom, respectively, and n is the number of dopant atoms ($n=1$ in this study). In the calculation of the formation energy, a bulklike environment is considered for Si atoms, and an isolated phosphorus atom is used for μ_{dopant} . Si-film-thickness evolution of the formation energy is presented in Fig. 3. From the data presented in this figure, the formation energy of core-doped 1.2 nm-thick Si film is

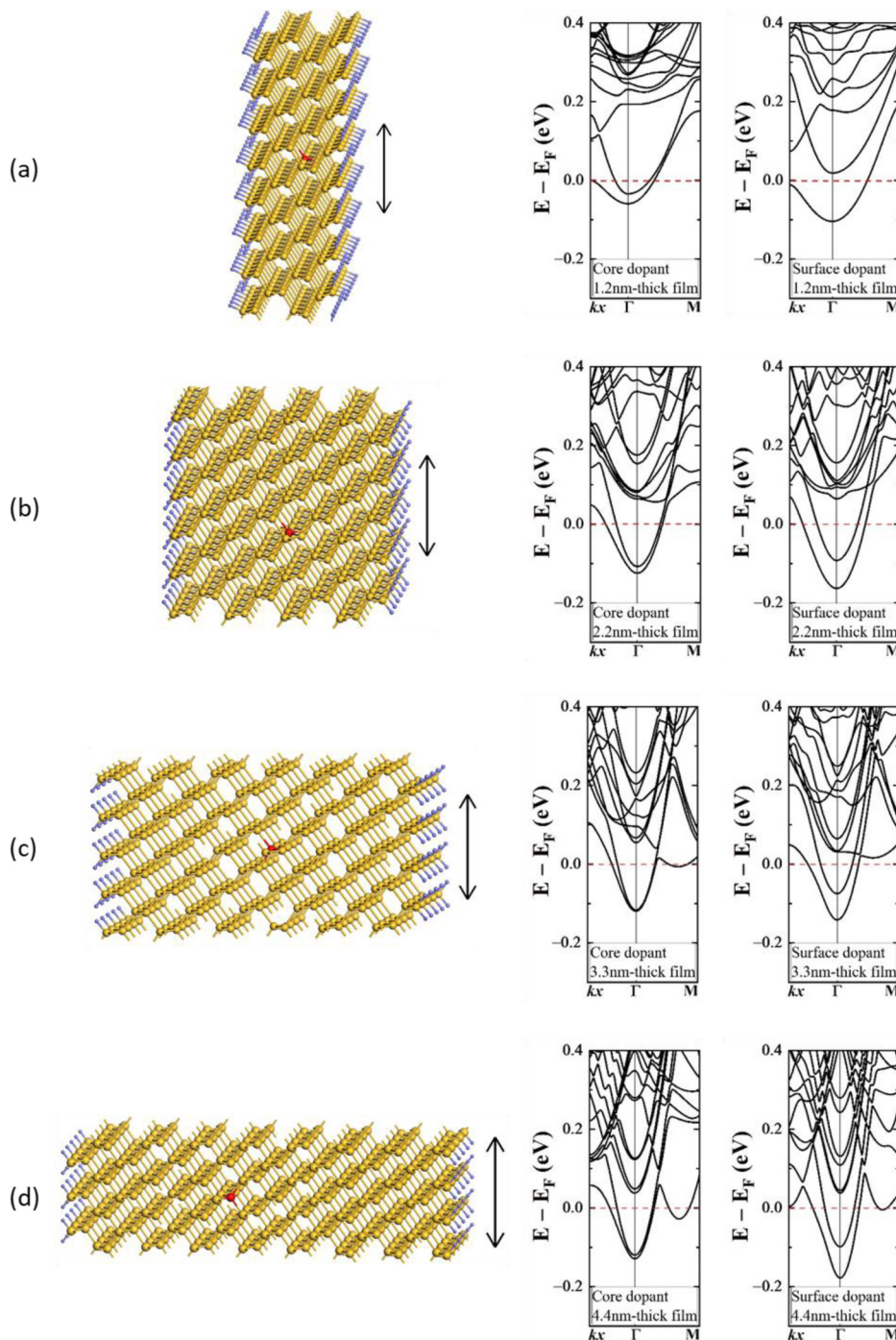


FIG. 2. Atomic illustration and conduction band structure of doped Si thin films. Left: atomic structure of hydrogen-terminated Si film with “core dopant” atom shown in red. Structures are periodic along the vertical arrows. Middle: conduction band structure of Si film considering “core dopant.” Right: conduction band structure of Si film considering “surface dopant.” Si films with identical volumes, along [100] orientation and with thicknesses of (a) 1.2 nm, (b) 2.2 nm, (c) 3.3 nm, and (d) 4.4 nm. Energies are referenced to the Fermi level (E_F). Doping concentration is $1.2 \times 10^{20} \text{ cm}^{-3}$. kx represents the edge of the Brillouin zone in the x -direction.

~ 0.5 eV larger than that of the bulk Si. As can also be observed, for both the “surface dopant” and “core dopant” structures, the formation energy increases with decreasing film thickness, i.e., it becomes increasingly more difficult to dope phosphorus atoms into

Si for thinner films. It can also be observed from Fig. 3 that the “surface dopant” structure is energetically more favorable compared to the “core dopant,” for all film thicknesses. Similar findings have been previously reported for boron-doped Si NWs.⁵² However, both

similar and opposite trends have been discussed in the literature for phosphorus-doped Si NWs.^{53–55} For comparison purposes, the formation energy of a phosphorus dopant in bulk Si and in Si NW with diameter of 1 nm is shown by red and green arrows, respectively, in this figure.

To evaluate detailed effects of dopants on the band structure and to be able to identify the bands created by the dopant, we studied a lower doping concentration. This is implemented by increasing the size of the supercell to $\sim 5 \times 5 \text{ nm}^2$ for the 1.2 nm film thickness, corresponding to $3 \times 10^{19} \text{ cm}^{-3}$ doping concentration. The band structure for both “surface dopant” and “core dopant” is shown in Figs. 4(a) and 4(b). The almost flat double bands with a dispersion of less than 55 meV are associated with the phosphorus dopant atom, as indicated by the projected DoS (PDoS) presented in Fig. 4(c) at energies around the dopant double bands. This figure shows that the dopant band is demonstrating the phosphorus character. The resonant dopant band could indicate that although the interaction between the dopants is suppressed, it is still strong enough to create a resonant state.⁵⁶ Charge difference density, which illustrates the charge distribution around the dopant atom, is shown in Fig. 4(d), where the red (green) distribution corresponds to charge accumulation (depletion).

Stronger quantum confinement and hence larger bandgap as a result of two-dimensional confinement, as well as further suppression of the long-range interaction between dopants and therefore reduced the charge periodic image, all due to 1D periodic boundary conditions in nanowire structures, allows using smaller supercell and therefore computationally achievable structures for identifying the dispersion-less dopant band. As a result, we also performed simulations considering Si NWs. Experiments have revealed that

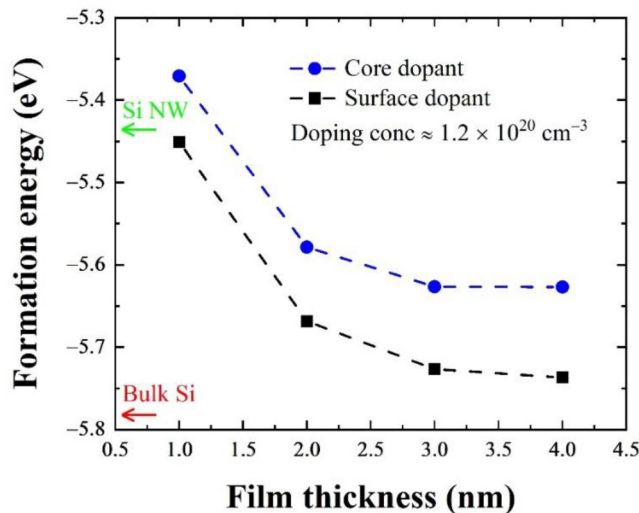


FIG. 3. Formation energy of doped Si nanostructures. Formation energy for a doping concentration of $1.2 \times 10^{20} \text{ cm}^{-3}$ for two dopant locations, i.e., surface dopant and core dopant, as functions of Si film thickness. The formation energy of a phosphorus dopant in bulk Si is shown by the red arrow. The green arrow points to the formation energy of phosphorus in the 1 nm-diameter Si NW.

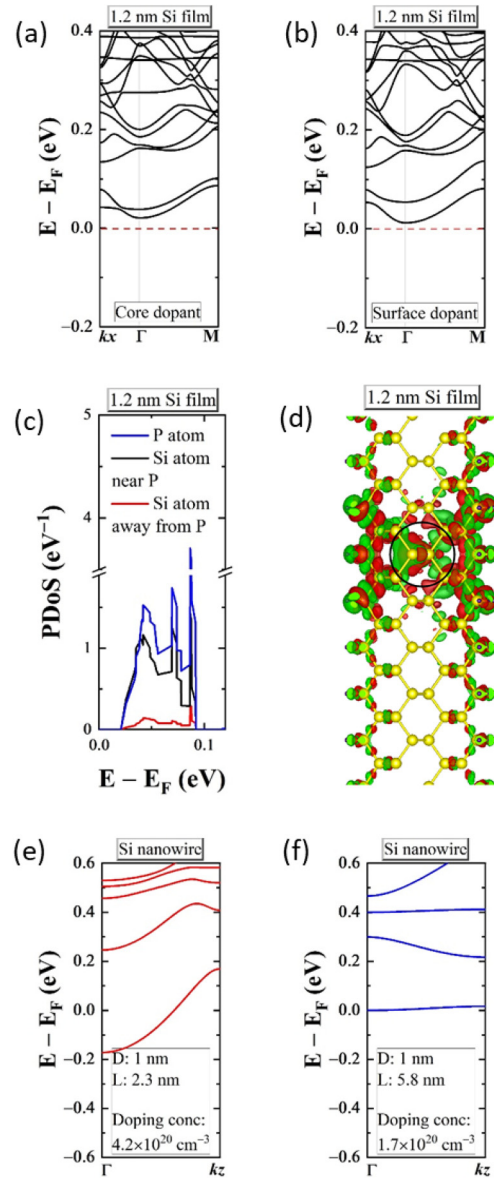


FIG. 4. Electronic structure properties of Si nanostructures. Dopant bands created near the Fermi energy of 1.2 nm-thick Si film for (a) “core dopant,” and (b) “surface dopant,” for doping concentration of $3 \times 10^{19} \text{ cm}^{-3}$. (c) Projected density of states (PDoS) of the phosphorus (P) dopant atom, a neighbouring Si atom, and a distanced Si atom, of the doped 1.2 nm-thick Si film showing that the dopant bands exhibit the phosphorus character. (d) Charge difference density of the doped 1.2 nm-thick Si film demonstrating the charge distribution at the dopant location (“core dopant structure”). Black circle shows the dopant location, and red (green) represents accumulation (depletion). Band structure of the doped Si nanowire (Si NW) with the length (L) of (e) 2.3 nm and (f) 5.8 nm and the diameter (D) of 1 nm for the given doping concentrations. Lower doping concentration in (f) allows an almost dispersion-less dopant band inside the bandgap. In (a), (b), (e), and (f) Energies are referenced to the Fermi level (E_F). kx in (a) and (b), and kz in (e) and (f) represent the edge of the Brillouin zone in the x - and z -direction, respectively.

synthesized Si NWs are produced predominantly oriented along the [110] crystal direction, particularly for diameters smaller than 10 nm.⁵⁷ Therefore, [110] orientation is considered in the construction of Si NWs in our calculations. The electronic structure of intrinsic 1 nm-diameter Si NW demonstrating a bandgap of 1.99 eV is depicted in Fig. S4 in the [supplementary material](#). The band structure of doped 1 nm-diameter Si NWs with lengths of 1.2 nm and 5.8 nm is shown in Figs. 4(e) and 4(f). As indicated in these two figures, the interaction between dopants in the NW structure is further suppressed for the 5.8 nm-long NW, and the dopant band dispersion is less than 15 meV. This allows us to extract a more accurate dopant activation energy. For the almost dispersion-less localized dopant band in the lower doped Si NW, the activation energy of ~ 200 meV is extracted. Band structures of the phosphorus-doped 1 nm-diameter Si NWs with different lengths, and hence different doping concentrations, are presented in Fig. S5 in the [supplementary material](#).

Analyzing the exact effects of the dopant atom-induced perturbation on the band structure of the Si thin film is very challenging. Using supercells in studying the effects of dopants is inevitable in DFT-based simulations. However, in addition to computational limitations, as the size of the supercell increases, the corresponding first Brillouin zone shrinks, and, as a result, bands of the supercell become extremely “folded” into the first Brillouin zone. Consequently, to be able to directly compare the folded bands with the reference band structure of a primitive cell, a procedure known as “unfolding” is required to unfold the primitive cell Bloch character hidden in the supercell eigenstates. By applying the unfolding procedure, the band structure of a supercell will be mapped to the band structure of a reference primitive cell.^{58,59} Utilizing a linear combination of atomic orbital basis sets in the presence of a perturbation, such as dopant, allows mapping of the symmetry breakers, which perturb the band structure.

To provide detailed insight into the effects of the phosphorus dopant on the band structure of the Si thin film, the unfolded band structures of the 1.2 nm-thick doped Si film for “core” and “surface” dopant locations are displayed as contour plots in Figs. 5(a) and 5(b), respectively, for a doping concentration of $1.2 \times 10^{20} \text{ cm}^{-3}$. States in the doped slab do not have a strictly defined wave vector because the translational symmetry has been broken by the dopant. Nevertheless, projecting the states in the presence of dopant, where the wave vector is not well-defined, onto the states without the dopant present, which do have the well-defined wave vector (two-dimensional momentum) ascribe a predominant momentum or a range of momenta that applied to the particular state from the dopant. In Fig. 5, the weight of this projection is illustrated, where the wave vector in the horizontal axis refers to the wave vector of the two-dimensional Brillouin zone, and the energy in the vertical axis refers to the energy of the states in the presence of dopant. The conduction band of the intrinsic Si film, presented earlier in Fig. 1(a), is shown by white dotted lines as reference in Fig. 5 and aligned to the conduction band edge of the doped structure, i.e., energies are referenced to the edge of conduction band (E_C). Unlike the bands presented in Figs. 2(a) and 2(b) for the doped Si films, the unfolded band structure offers a significant advantage of enabling direct comparison with the corresponding intrinsic counterpart. This allows detailed evaluation of the hybridization of the

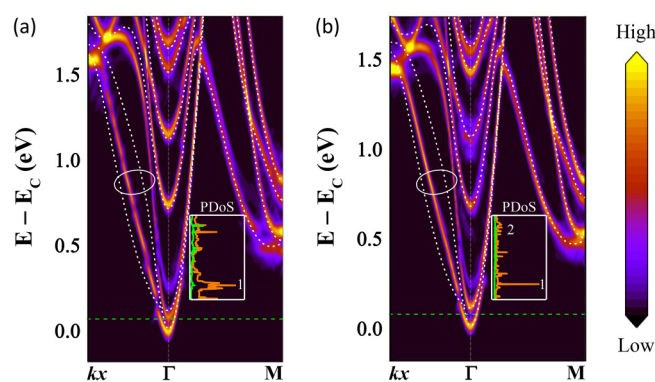


FIG. 5. Unfolded band structure of doped Si ultra-thin film. Unfolded band structure of doped 1.2 nm-thick Si film for (a) “core,” and (b) “surface” dopants with the concentration of $1.2 \times 10^{20} \text{ cm}^{-3}$ shown using contour plots of total weight intensity as a function of wave vector in the two-dimensional Brillouin zone. Yellow and black represent the two extremes of high and low spectral weights, respectively, where the bright colours correspond to unchanged bands compared to the intrinsic structure without the dopant, i.e., large overlap. The intrinsic Si film conduction band is shown using white dashed lines which is the same as in Fig. 1(a) and is aligned to the conduction band edge of the doped film as reference, i.e., energies are referenced to conduction band edge (E_C). Insets show the projected density of states (PDoS) of the phosphorus dopant atom (in orange) and a Si atom away from the dopant (in green), at energies linked to the energy axis of the contour plots. 1 and 2 indicate dopant-induced states and the contribution of the phosphorus dopant compared to that of the Si atom. Regions shown by white ovals in Γ - kx space are strongly perturbed by the dopant. Horizontal green dashed lines show the Fermi energy of the doped Si film. kx represents the edge of the Brillouin zone in the x -direction.

dopant band with the Si conduction band, as well as clearly identifying dopant bands that demonstrate dispersing feature due to the limited distance between dopants. Specifically, our calculation yields dopant-induced energy bands at $E - E_C \approx 0.25 \text{ eV}$ and 0.17 eV (at the Γ -valley) for core and surface dopant locations, respectively, for such high carrier concentration indicating a degenerate condition. In addition, it can be observed that an extra energy band is created at $E - E_C \approx 0.5 \text{ eV}$ (at the Γ -valley) for the surface dopant. It is also evident that although the dopant does some scrambling of the momentum in regions around the M-valley, the states are not strongly affected by the presence of the dopant, i.e., unperturbed, with energies that closely track the unperturbed bands (white dashed lines) and with a sharp peak of the spectral weight. Rather remarkably, dopant has a substantial effect on the bands in the Γ - kx space, where the states are rather strongly perturbed by the dopant, in contrast to the M-point (shown by white ovals). Insets of Figs. 5(a) and 5(b) demonstrate projected density of states (PDoS) of the dopant atom and an Si atom away from the dopant, in orange and green, respectively. Clear distinctions can be observed between strong peaks, and hence, contribution of the dopant atom and a rather minimal contribution of the Si atom, to the states that correspond to the dopant bands created at energies around the PDoS peaks, labeled as 1 and 2. Moreover, as can be conspicuously seen by comparing Figs. 5(a) and 5(b), the unfolding method reveals less density of states at the Fermi energy (shown by green horizontal

dashed lines for the doped structures) for the surface dopant than the core dopant, consistent with Figs. 2(a) and S4 in the supplementary material.

EXPERIMENTAL INVESTIGATION

In order to evaluate our theoretical predictions, SOI wafers have been fabricated to experimentally investigate the doping characteristic of phosphorus-doped ultra-thin Si films. For this purpose, SOI wafers with nominally 66 nm undoped Si [100] on 145 nm of buried oxide were used to obtain ultra-thin Si films. The SOI was thinned by performing cyclic steps of dry oxidation in a furnace at 1000 °C and oxide etching through ozone-cleaning to uniformly remove controlled amounts of Si using ozone gas, ammonium hydroxide, and hydrofluoric acid in a spray acid tool for preoxidation wafer cleaning.⁵⁰ Ion implantation has been employed at room temperature to introduce dopants with a phosphorus energy of 2 keV, a dose of $1 \times 10^{15} \text{ cm}^{-2}$, and 7° beam-line. The SOI wafer has then gone through a 5-s post-implantation anneal at 1050 °C in nitrogen ambient. It is expected that the thermal budget of the RTA would be sufficient to effectively remove ion implant-related defects in the ultra-thin SOI film. Cross-sectional transmission electron microscopy (XTEM) confirms the uniformity of the final SOI and the thickness to be 4.5 nm [see Fig. 6(a)]. No typical related defect has been observed in the XTEM analysis. “Control” bulk Si samples from a nominally undoped Si wafer were loaded in the ion implanter together with the SOI samples to enable evaluating the incorporation of dopants in Si. Electrochemical capacitance voltage (ECV) characterization was then carried out using the

control bulk samples to identify the active doping concentration as a function of Si depth using a wafer profiler (WEP CVP21, area: $1.1 \times 10^{-6} \text{ m}^2$). The ECV profile presented in Fig. 6(a) confirms that on a bulk Si control sample, the active concentration peaked close to $1 \times 10^{20} \text{ cm}^{-3}$.

To evaluate the electrical properties of the 4.5 nm doped SOI film, circular transfer length method (CTLM) structures were defined using photolithography and Ti/Au (10 nm/90 nm) metal evaporation, followed by the standard lift-off process. Repeated sets of identical, i.e., 25 μm diameter, inner circular electrodes with concentric but different diameter outer contacts were patterned, resulting in various gaps between the inner and the outer electrodes. A parameter analyzer (Agilent B1500) in a probe station (cascade semi-automatic prober) was setup to perform electrical measurements. The voltage was swept in 20 mV increments from -1 V to +1 V. Electrical measurements are performed at different temperatures from -50 °C to 75 °C with 25 °C increments. The dopant activation energy (E_A), as one of the key parameters to correlate the theoretical predictions with the experimental results, can be obtained from the variation of the current at a given bias vs temperature. The experimentally obtained activation energy is an accumulation of different physical effects happening at the same time as temperature changes.⁶⁰ More specifically, current is proportional to the product of carrier concentration, n , and carrier mobility, μ , both of which are temperature dependent, i.e.,

$$I(T) \propto n(T) \times \mu(T), \quad (2)$$

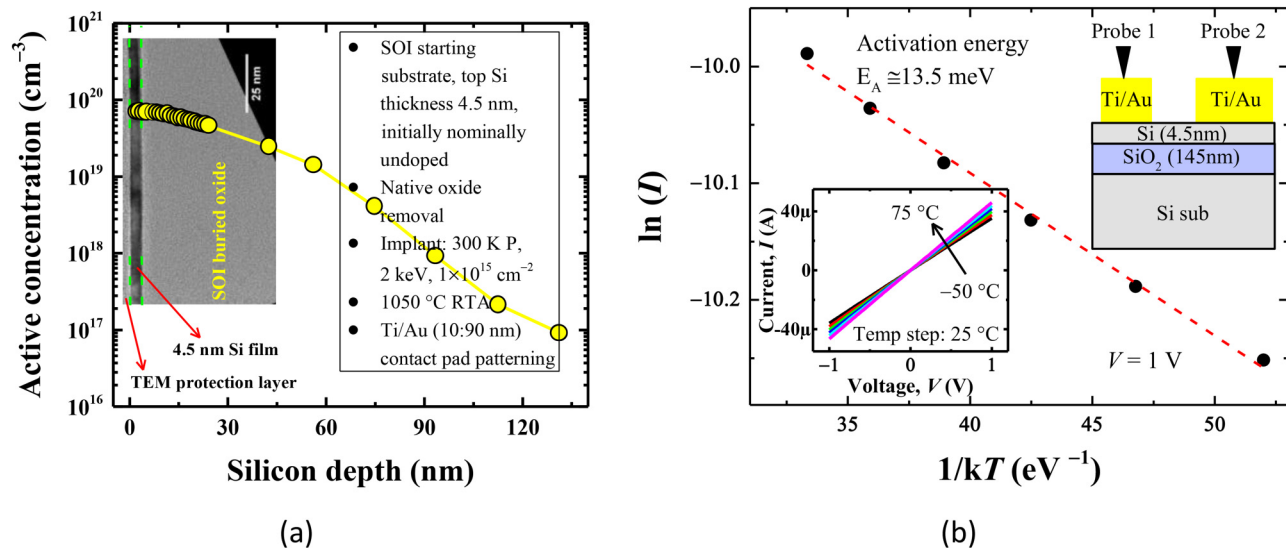


FIG. 6. Phosphorus-doped uSOI wafer by ion implantation. (a) ECV profile of nominally un-doped Si sample used for the same phosphorus ion implantation demonstrating the active concentration peaked close to $1 \times 10^{20} \text{ cm}^{-3}$. XTEM image at the background confirms the SOI thickness to be 4.5 nm. Scale of the XTEM image is kept the same as the ECV profile to allow identifying the active concentration level in the Si film. Fabrication steps are listed as inset. (b) Temperature-dependent current at a given bias of 1 V. Upper inset illustrates the schematic of the fabricated devices. Lower inset shows linear I-Vs for the measured temperatures from -50 °C to 75 °C. Activation energy (E_A) is obtained from the linear fit shown by red dashed line. Similar activation energy values (13.4 meV and 13.6 meV) have been extracted from structures with different distance between the two contacts, demonstrating negligible effect of the contact resistance compared to the doped Si film resistance.

with associated activation energies of $E_{A,n}$ and $E_{A,p}$, respectively. Current–voltage (I – V) plots of a typical CTLM contact at different temperatures are shown as the inset of Fig. 6(b). As can be seen in this figure, current increases with temperature indicating that the product of carrier concentration \times mobility is increasing with temperature. Since the doped Si film is ultra-thin, i.e., 4.5 nm, and formed by oxidation and etching, it is anticipated that the mobility will be surface roughness scattering (SRS) limited,^{61,62} which is approximately independent of temperature ($E_{A,\mu} \approx 0$ eV), or decrease with increasing temperature ($E_{A,\mu} < 0$ eV), as reported in Refs. 63–65. In the former case, the dopant activation energy would effectively be the same as the extracted activation energy from temperature-dependent I – V , i.e., $E_{A,n} = E_A$. In the latter case, however, the effective dopant activation energy would be larger than the extracted one, i.e., $E_{A,n} > E_A$. As depicted in this figure, the effective activation energy extracted from the linear fit of the temperature-dependent I – V is ~ 13.5 meV (“close-to-degenerate” condition). It is worth mentioning that a probable small inaccuracy in the ECV profile would lead to the overestimation of the actual carrier concentration in the doped uSOI. Note that the ECV measurements have been performed on the bulk Si wafers and it is expected that the back interface of the SOI, i.e., Si/SiO₂ interface, would trap dopants. As a result, the active concentration is expected to be less in the SOI compared to the bulk Si. Nevertheless, the experimentally achieved “close-to-degeneracy” condition is consistent with our theoretical predictions for comparable film thickness and slightly higher doping concentration of 1.2×10^{20} cm^{−3} [see Fig. 2(d)], where the Fermi level is in the conduction band. Due to the competing phenomena affecting the current conduction, additional characterization and analysis such as temperature-dependent van-der-Pauw Hall measurements of the SOI film could be the subject of future study.

CONCLUSIONS

In conclusion, this work presents a combined theoretical and experimental study of the doping behavior of ultra-thin Si films. Through our first-principles calculations, two doping concentrations in sub-5 nm Si films and 1 nm-diameter Si nanowires with different lengths have been studied, taking into account quantum confinement effects. Smaller quantum confinement-induced bandgap widening has been observed in thin films compared to nanowires, as expected. Our calculated dopant formation energy revealed that doping becomes more difficult as the film thickness decreases. It has also been demonstrated that the surface dopant has smaller formation energy, i.e., technologically easier to achieve; however, it generates less density of states compared to the core dopant. A broader implication of this result is that it may fundamentally require the industry to re-evaluate doping methodologies for future thin film and nanowire device technologies. A direct comparison between folded bands of the doped Si films and the reference band structure of the intrinsic film has been enabled through applying the unfolding procedure. As a result, the dopant band has been identified and hybridization of the Si band structure due to phosphorus dopant has been revealed. *Ex situ* doping of SOI wafers has been carried out using ion implantation to experimentally dope ultra-thin 4.5 nm Si films. CTLM structures have been realized using the doped SOI wafers. The effective dopant activation energy extracted from temperature-dependent

electrical characterization of the CTLM structures is ~ 13.5 meV. Remarkable agreement between our simulation and experiment has been achieved considering the meta-GGA corrected band structure resulting in considerable improvement in predicting the Si bandgap. Our experimental results demonstrate achieving active carrier concentration in ultra-thin Si films to near degenerate level, critical in the realization of the next-generation ultra-scaled fin-FET technology.

SUPPLEMENTARY MATERIAL

See the [supplementary material](#) for additional details of the electronic structure of intrinsic and doped Si nanostructures.

ACKNOWLEDGMENTS

This work is supported by the European Union’s Horizon 2020 Research and Innovation program via the ASCENT Access Network (Grant Agreement No. 654384). SFI/HEA Irish Centre for High-End Computing (ICHEC) is acknowledged for the provision of computational facilities and support. L.A. and A.C. would also like to acknowledge funding from Irish Research Council (IRC) through Award Nos. GOIPD/2018/653 and EPSPG/2017/356.

DATA AVAILABILITY

The data that support the findings of this study are available from the corresponding author upon reasonable request.

REFERENCES

- ¹G. E. Moore, “Cramming more components onto integrated circuits,” *Electronics* **38**, 114–117 (1965).
- ²L. Ansari, G. Fagas, and J. C. Greer, *Appl. Phys. Lett.* **105**, 123105 (2014).
- ³J.-P. Colinge, *Solid-State Electron.* **48**, 897 (2004).
- ⁴ITRS, see <http://www.itrs2.net> for semiconductor technology trends and projections.
- ⁵Fermi wavelength in semiconductors is several orders of magnitude larger than the interatomic distance, depending on the carrier effective mass and temperature.
- ⁶D. Akinwande, C. Huyghebaert, C.-H. Wang, M. I. Serna, S. Goossens, L.-J. Li, H.-S. P. Wong, and F. H. L. Koppens, *Nature* **573**, 507 (2019).
- ⁷R. Merritt, EE Times, see <https://go.nature.com/2rh4pzh> (24 April 2019).
- ⁸Samsung Newsroom, see <https://go.nature.com/2sygF5F> (16 April 2019).
- ⁹L. Ansari, B. Feldman, G. Fagas, J.-P. Colinge, and J. C. Greer, *Appl. Phys. Lett.* **97**, 062105 (2010).
- ¹⁰S. Migita, Y. Morita, M. Masahara, and H. Ota, *Jpn. J. Appl. Phys.* **52**, 04CA01 (2013).
- ¹¹S. Goswami, K. A. Slinker, M. Friesen, L. M. McGuire, J. L. Truitt, C. Tahan, L. J. Klein, J. O. Chu, P. M. Mooney, D. W. van der Weide, R. Joynt, S. N. Coppersmith, and M. A. Eriksson, *Nat. Phys.* **3**, 41 (2007).
- ¹²B. Hensen, W. Wei Huang, C.-H. Yang, K. Wai Chan, J. Yoneda, T. Tanttu, F. E. Hudson, A. Laucht, K. M. Itoh, T. D. Ladd, A. Morello, and A. S. Dzurak, *Nat. Nanotechnol.* **15**, 13 (2020).
- ¹³L. Petit, H. G. J. Eenink, M. Russ, W. I. L. Lawrie, N. W. Hendrickx, S. G. J. Philips, J. S. Clarke, L. M. K. Vandersypen, and M. Veldhorst, *Nature* **580**, 355 (2020).
- ¹⁴B. Lloyd, M. Smith, Z. Gong, and M. Singh, in *Bulletin of the American Physical Society APS March Meeting March 2–6, 2020* (APS, 2020).
- ¹⁵A. Dzurak, *Nat. Electron.* **2**, 266 (2019).
- ¹⁶L. Bourdet, L. Hutin, B. Bertrand, A. Corna, H. Bohuslavskyi, A. Amise, A. Crippa, R. Maurand, S. Barraud, M. Urdampilleta, C. Bäuerle, T. Meunier,

- M. Sanquer, X. Jehl, S. D. Franceschi, Y. Niquet, and M. Vinet, *IEEE Trans. Electron Devices* **65**, 5151 (2018).
- ¹⁷M. Vinet, L. Hutin, B. Bertrand, S. Barraud, J. Hartmann, Y. Kim, V. Mazzocchi, A. Amisse, H. Bohuslavskyi, L. Bourdet, A. Crippa, X. Jehl, R. Maurand, Y. Niquet, M. Sanquer, B. Venitucci, B. Jadot, E. Chanrion, P. Mortemousque, C. Spence, M. Urdampilleta, S. D. Franceschi, and T. Meunier, *Towards Scalable Silicon Quantum Computing* (IEEE, 2018), p. 6.5.1.
- ¹⁸T. Chen, J. van Gelder, B. van de Ven, S. V. Amitonov, B. de Wilde, H.-C. Ruiz Euler, H. Broersma, P. A. Bobbert, F. A. Zwanenburg, and W. G. van der Wiel, *Nature* **577**, 341 (2020).
- ¹⁹P. Pichler, *Intrinsic Point Defects, Impurities, and Their Diffusion in Silicon* (Springer, Berlin, 2004).
- ²⁰T. Hiramoto, *Nat. Electron.* **2**, 557 (2019).
- ²¹G. Seguíni, C. Castro, S. Schamm-Chardon, G. BenAssayag, P. Pellegrino, and M. Perego, *Appl. Phys. Lett.* **103**, 023103 (2013).
- ²²D. König, D. Hiller, S. Gutsch, and M. Zacharias, *Adv. Mater. Interfaces* **1**, 1400359 (2014).
- ²³M. Perego, G. Seguíni, E. Arduca, J. Frascaroli, D. De Salvador, M. Mastromatteo, A. Carnera, G. Nicotra, M. Scuderi, C. Spinella, G. Impellizzeri, C. Lenardi, and E. Napolitani, *Nanoscale* **7**, 14469 (2015).
- ²⁴D. König, S. Gutsch, H. Gnaser, M. Wahl, M. Kopnarski, J. Göttlicher, R. Steininger, M. Zacharias, and D. Hiller, *Sci. Rep.* **5**, 9702 (2015).
- ²⁵D. Hiller, J. López-Vidrier, S. Gutsch, M. Zacharias, K. Nomoto, and D. König, *Sci. Rep.* **7**, 863 (2017).
- ²⁶E. Arduca, G. Seguíni, C. Martella, A. Lamperti, E. Napolitani, D. De Salvador, G. Nicotra, M. Scuderi, C. Spinella, and M. Perego, *J. Mater. Chem. C* **6**, 119 (2018).
- ²⁷R. Rurali, *Rev. Mod. Phys.* **82**, 427 (2010).
- ²⁸D. K. Schroder, *Semiconductor Material and Device Characterization* (John Wiley & Sons, Inc., 2006), Chap. 3, p. 127.
- ²⁹QuantumATK, version 2017.2, Synopsys QuantumATK, see <https://www.synopsys.com/silicon/quantumatk.html>.
- ³⁰J. P. Perdew and A. Zunger, *Phys. Rev. B* **23**, 5048 (1981).
- ³¹T. Ozaki and H. Kino, *Phys. Rev. B* **69**, 195113 (2004).
- ³²D. Sharma, L. Ansari, B. Feldman, M. Iakovidis, J. C. Greer, and G. Fagas, *J. Appl. Phys.* **113**, 203708 (2013).
- ³³L. Ansari, B. Feldman, G. Fagas, C. M. Lacambra, M. G. Haverty, K. J. Kuhn, S. Shankar, and J. C. Greer, *IEEE Trans. Nanotechnol.* **12**, 1075 (2013).
- ³⁴H. J. Monkhorst and J. D. Pack, *Phys. Rev. B* **13**, 5188 (1976).
- ³⁵F. Tran and P. Blaha, *Phys. Rev. Lett.* **102**, 226401 (2009).
- ³⁶L. Ansari, F. Gity, and J. C. Greer, *J. Phys.: Condens. Matter* **29**, 065301 (2017).
- ³⁷L. Ansari, G. Fagas, J.-P. Colinge, and J. C. Greer, *Nano Lett.* **12**, 2222 (2012).
- ³⁸F. Gity, L. Ansari, C. König, G. A. Verni, J. D. Holmes, B. Long, M. Lanius, P. Schüffegen, G. Mussler, D. Grützmacher, and J. C. Greer, *Microelectron. Eng.* **195**, 21 (2018).
- ³⁹F. Gity, L. Ansari, M. Lanius, P. Schüffegen, G. Mussler, D. Grützmacher, and J. C. Greer, *Appl. Phys. Lett.* **110**, 093111 (2017).
- ⁴⁰T.-L. Chan, M. L. Tiago, E. Kaxiras, and J. R. Chelikowsky, *Nano Lett.* **8**, 596 (2008).
- ⁴¹A. Carvalho, S. Öberg, M. Barroso, M. J. Rayson, and P. Briddon, *Phys. Status Solidi A* **209**, 1847 (2012).
- ⁴²R. Guerra and S. Ossicini, *J. Am. Chem. Soc.* **136**, 4404 (2014).
- ⁴³Z. Ni, X. Pi, and D. Yang, *Phys. Rev. B* **89**, 035312 (2014).
- ⁴⁴W. D. A. M. de Boer, D. Timmerman, K. Dohnalová, I. N. Yassievich, H. Zhang, W. J. Buma, and T. Gregorkiewicz, *Nat. Nanotechnol.* **5**, 878 (2010).
- ⁴⁵D. Liang and J. E. Bowers, *Nat. Photonics* **4**, 511 (2010).
- ⁴⁶M. Fuechsle, J. A. Miwa, S. Mahapatra, H. Ryu, S. Lee, O. Warschkow, L. C. L. Hollenberg, G. Klimeck, and M. Y. Simmons, *Nat. Nanotechnol.* **7**, 242 (2012).
- ⁴⁷D. J. Norris, A. L. Efros, and S. C. Erwin, *Science* **319**, 1776 (2008).
- ⁴⁸Y. He, S. K. Gorman, D. Keith, L. Kranz, J. G. Keizer, and M. Y. Simmons, *Nature* **571**, 371 (2019).
- ⁴⁹L. Ansari, B. Feldman, G. Fagas, J.-P. Colinge, and J. C. Greer, *Solid-State Electron.* **71**, 58 (2012).
- ⁵⁰J. MacHale, F. Meaney, N. Kennedy, L. Eaton, G. Mirabelli, M. White, K. Thomas, E. Pelucchi, D. H. Petersen, R. Lin, N. Petkov, J. Connolly, C. Hatem, F. Gity, L. Ansari, B. Long, and R. Duffy, *J. Appl. Phys.* **125**, 225709 (2019).
- ⁵¹M. Diarra, Y.-M. Niquet, C. Delerue, and G. Allan, *Phys. Rev. B* **75**, 045301 (2007).
- ⁵²M.-F. Ng, M. B. Sullivan, S. W. Tong, and P. Wu, *Nano Lett.* **11**, 4794 (2011).
- ⁵³H. Peelaers, B. Partoens, and F. M. Peeters, *Nano Lett.* **6**, 2781 (2006).
- ⁵⁴M. Amato, S. Ossicini, E. Canadell, and R. Rurali, *Nano Lett.* **19**, 866 (2019).
- ⁵⁵J. Han, T.-L. Chan, and J. R. Chelikowsky, *Phys. Rev. B* **82**, 153413 (2010).
- ⁵⁶F. Bassani, G. Iadonisi, and B. Preziosi, *Rep. Prog. Phys.* **37**, 1099 (1974).
- ⁵⁷N. P. Dasgupta, J. Sun, C. Liu, S. Brittman, S. C. Andrews, J. Lim, H. Gao, R. Yan, and P. Yang, *Adv. Mater.* **26**, 2137 (2014).
- ⁵⁸W. Ku, T. Berlijn, and C.-C. Lee, *Phys. Rev. Lett.* **104**, 216401 (2010).
- ⁵⁹C.-C. Lee, Y. Yamada-Takamura, and T. Ozaki, *J. Phys.: Condens. Matter* **25**, 345501 (2013).
- ⁶⁰R. Duffy, A. Heringa, V. C. Venezia, J. Loo, M. A. Verheijen, M. J. P. Hopstaken, K. van der Tak, M. de Potter, J. C. Hooker, P. Meunier-Beillard, and R. Delhougne, *Solid-State Electron.* **54**, 243 (2010).
- ⁶¹X. He, J. Fronheiser, P. Zhao, Z. Hu, S. Uppal, X. Wu, Y. Hu, R. Sporer, L. Qin, R. Krishnan, E. M. Bazizi, R. Carter, K. Tabakman, A. K. Jha, H. Yu, O. Hu, D. Choi, J. G. Lee, S. B. Samavedam, and D. K. Sohn, in *2017 IEEE International Electron Devices Meeting, San Francisco, CA, 2-6 December 2017* (IEEE, New York, 2017).
- ⁶²M. J. H. v. Dal, N. Collaert, G. Doornbos, G. Vellianitis, G. Curatola, B. J. Pawlak, R. Duffy, C. Jonville, B. Degroote, E. Altamirano, E. Kunnen, M. Demand, S. Beckx, T. Vandeweyer, C. Delvaux, F. Leys, A. Hikavy, R. Rooyackers, M. Kaiser, R. G. R. Weemaes, S. Biesemans, M. Jurczak, K. Anil, L. Witters, and R. J. P. Lander, in *2007 IEEE Symposium on VLSI Technology*, 12-14 June 2007, Kyoto (IEEE, New York, 2007).
- ⁶³D. Esseni, M. Mastrapasqua, G. K. Celler, C. Fiegna, L. Selmi, and E. Sangiorgi, *IEEE Trans. Electron Devices* **48**, 2842 (2001).
- ⁶⁴K. Uchida, J. Koga, and S.-i. Takagi, *J. Appl. Phys.* **102**, 074510 (2007).
- ⁶⁵M. Auslender and S. Hava, in *Springer Handbook of Electronic and Photonic Materials*, edited by S. Kasap and P. Capper (Springer, Cham, 2017).